

¹ Molecular Design of Dispersed Nickel Phthalocyanine@Nanocarbon ² Hybrid Catalyst for Active and Stable Electroreduction of CO₂

³ Published as part of *The Journal of Physical Chemistry* virtual special issue “Energy and Catalysis in China”.

⁴ Zisheng Zhang and Yang-Gang Wang*



Cite This: <https://doi.org/10.1021/acs.jpcc.1c02508>



Read Online

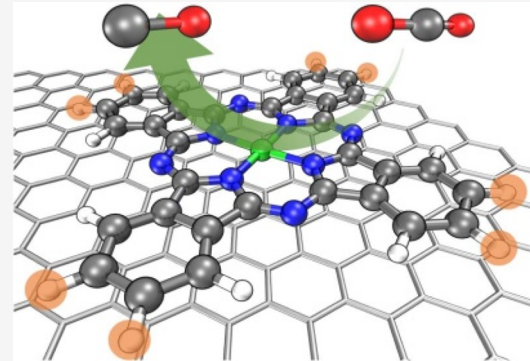
ACCESS |

Metrics & More

Article Recommendations

Supporting Information

5 ABSTRACT: The molecular catalyst/nanocarbon hybrid through $\pi-\pi$
6 stacking immobilization is an emerging family of single-atom catalysts with
7 outstanding performance in electrocatalysis, well-defined active site, and
8 tunability at molecular level through functional group substitution. In the
9 present work, we provide a general strategy for the rational design of molecular
10 single-atom catalyst in the form of nickel phthalocyanine@nanocarbon
11 (NiPc@NC) for highly efficient electroreduction of CO₂ to CO. We employ
12 density functional theory (DFT) calculations and state-of-the-art electronic
13 structure analysis to explore the mechanism and substituent effects on
14 structural stability, redox chemistry, adsorption properties, and molecule–
15 substrate interactions of the NiPc catalyst. We have revealed that the electron-
16 withdrawing groups facilitate the reductive activation of the catalytic Ni center
17 but weaken the Ni–N bond strength and make the CO desorption sluggish,
18 while the electron-donating groups do the opposite. A substituent-dependent correlation between interaction strength and electron
19 transfer through the interface is also revealed by noncovalent interaction analysis and electron density difference projection. On the
20 basis of the gained insights, we apply semiempirical quantum mechanical (SQM) calculation, machine learning (ML), and genetic
21 algorithm (GA) to screening through the chemical space of ca. 10 trillion substituted NiPc molecules under a descriptor scheme to
22 identify promising molecular candidates for the NiPc@NC hybrid material. The best candidate from GA search outperforms the
23 state-of-the-art catalyst in terms of stability, reduction potential (improved by 100 mV), and interaction with substrate (strengthened
24 by 0.46 eV). Design strategies are proposed based on the top-scoring molecules from computational screening, and the workflow is
25 highly generalizable and transferable to similar molecular systems for other applications.



26 ■ INTRODUCTION

27 The climbing carbon emission worldwide has been intensifying
28 the greenhouse effect which poses a threat to ecosystems and
29 causes extreme weather conditions all over the globe.¹ It is
30 more than crucial for humanity to develop a sustainable and
31 environmentally friendly energy infrastructure which can
32 properly close the carbon cycle of ecosystems. The CO₂
33 reduction reaction (CO₂RR) is the most straightforward and
34 scalable way to convert carbon dioxide into value-added
35 chemicals using surplus renewable energy and hence is one of
36 the most promising technologies in the field of environmental
37 and energy science.² The gaseous products of such a reaction,
38 including CO, CH₄, C₂H₄, and so on, can be easily separated
39 from the reaction system and are important building blocks of
40 chemical industry and pharmaceuticals.³ However, few electro-
41 catalysts, other than noble-metal-based materials (e.g., Pt, Au,
42 IrO₂, and RuO₂), can meet the demand of practical application
43 in terms of kinetics, selectivity, and stability.^{3,4} Therefore, it is
44 critical to develop electrocatalysts based on earth-abundant
45 transition metals (TM) with performance comparable to that
46 of noble metals.

In the recent decade, the study of single-atom catalysts⁴⁷ (SACs) is a rapidly growing hot spot in electrocatalysis.^{5–7} By⁴⁸ embedding transition metal atoms into a conducting matrix⁴⁹ such as nanostructured carbon materials, the electrocatalysts⁵⁰ can achieve atomic dispersion which not only drastically boosts⁵¹ the atomic efficiency but also provides a platform for⁵² mechanistic study utilizing operando characterization techniques.^{8–11} However, those SAC are usually derived from the⁵⁴ pyrolysis of a carbon-containing precursor or a wet⁵⁵ impregnation method, which usually suffers from the sintering⁵⁶ of metal atoms into clusters or nanoparticles (that requires an⁵⁷ additional removal step).¹² Moreover, it is rather difficult to⁵⁸

Received: March 19, 2021

Revised: May 17, 2021

59 fine-tune the local electronic structure since there is not exact
60 control of doping position in the preparation process.

61 In terms of an atomic-level understanding of the active site
62 and manipulatable local environment, molecular systems,
63 especially transition metal phthalocyanines and porphins,
64 could outperform SACs since their geometric and electronic
65 structures are more well-defined;^{13,14} hence, one can make
66 modifications to it by substituent or through-space effects
67 based on an understanding of the electronic structure–activity
68 relationship to improve its property toward a certain optimum,
69 i.e., molecular engineering.^{15–18} The concept has been widely
70 applied to various energy applications including solar cells,¹⁹
71 redox flow cells,²⁰ molecular photocatalysis,²¹ and homoge-
72 neous electrocatalysis.^{22–24} In the recent decades, with the
73 development of low-cost quantum mechanical methods,
74 researchers are able to simulate over-large molecular libraries
75 by high-throughput virtual screening.²⁵ The low-cost quantum
76 mechanical methods or predictive machine learning (ML)
77 models, when coupled with a proper molecular representation
78 and evolutionary algorithms, make extremely efficient possible
79 optimization of a certain molecular property in any predefined
80 chemical subspace, with minimal human interference.²⁶

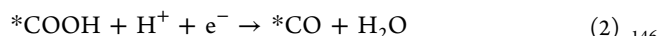
81 Although there has been exciting progress in rational or
82 inverse design of molecular electrocatalysts, due to sluggish
83 charge transfer kinetics with the electrode, efforts have been
84 made to immobilize molecular electrocatalysts onto an electric
85 conducting substrate to achieve heterogenization.^{27,28} This
86 family of heterogeneous molecular catalysts, also featuring
87 atomically dispersed active sites, have been accepted as
88 SACs.^{29,30} However, many studies adopt covalent immobiliza-
89 tion approaches which may introduce structural changes to the
90 molecular catalysts. To avoid such an effect, immobilization
91 through noncovalent $\pi-\pi$ stacking is one of the most
92 successful techniques to anchor a macrocyclic metal complex
93 on heterogeneous conducting carbon substrate. In 2017, Liang
94 and co-workers reported the noncovalent immobilization of
95 molecularly engineered cobalt phthalocyanine (CoPc) onto
96 carbon nanotubes (CNTs) via $\pi-\pi$ stacking to achieve 98%
97 faradaic efficiency (FE) toward a selective CO₂RR to CO with
98 superior activity.³¹ Moreover, the noncovalent interaction it
99 utilizes to achieve immobilization prevents the supported metal
100 complex from structural changes, allowing preservation of the
101 molecular integrity and fine-tuning of the electronic structure
102 of the SA sites at atomic scale. In our recent work, a rationally
103 designed nickel phthalocyanine (NiPc)-OMe@CNT hybrid
104 achieved unit conversion to CO with high current density, and
105 tetramethoxy substitution improves the stability of NiPc, which
106 suffers from deactivation in its pristine form.³² Recently, Liu
107 and co-workers also demonstrated that NiPc-NH₂@CNT to
108 be an efficient and selective electrocatalysis for electrochemical
109 reduction of CO₂ to CO.³³ The combined multiscale
110 engineering approach provides a clear and efficient strategy
111 toward the rational design of SAC for electrocatalytic
112 applications and emerges as a promising platform for
113 experimental and computational studies of electrocatalytic
114 mechanisms.

115 In this study, we focus on the use of NiPc for CO₂RR since
116 its reaction pathway is not altered after substitution with even
117 strong electron-withdrawing groups (EWG) and electron-
118 donating groups (EDG), unlike CoPc which branches into a
119 CH₄ pathway when EDG is introduced.³⁴ The reaction
120 mechanism of the CO₂RR to CO on NiPc is discussed with
121 density functional theory (DFT) calculations. The bonding

122 mode and interaction between adsorbate and nickel center are
123 investigated in depth with extensive wave function analysis and
124 energy decomposition analysis. After understanding the
125 molecular system, we take a few steps further into the realistic
126 realm to evaluate the effect of interaction between NiPc and
127 the nanocarbon substrate and the through-space electron
128 transfer across the $\pi-\pi$ stacking interface. On the basis of these
129 understandings, we performed computational screening
130 combining genetic algorithm (GA), semiempirical quantum
131 mechanical (SQM) calculation, and a deep neural network
132 (NN) model to explore the chemical space of substituted
133 nickel phthalocyanines. The top-scoring candidate molecules
134 are reported, and several design strategies are concluded from
135 the computational screening.
136

METHODS

The CO₂RR is studied under the computational hydrogen electrode (CHE) scheme³⁵ where the electron and proton transfer steps are treated as coupled, and the zero voltage is defined based on the reversible hydrogen electrode under standard condition. The effect of applied bias on a proton–electron transfer step is represented by adding a $-eU$ term to the standard ΔG. The CO₂RR pathways are listed below (where * stands for the active site):
144



DFT calculations on isolated molecules (nickel phthalocyanines, H₂, H₂O, CO₂, and CO) are performed using Gaussian 16, A.03 edition,³⁶ PBE0 functional³⁷ with D3 correction (Becke–Johnson damping)³⁸ is adopted for its robustness and dispersion corrections which make it widely accepted as proper functional to study reaction energetics of transition metal complexes. The Stuttgart–Dresden (SDD) basis set, containing all double-ξ valence with effective core potentials (ECPs), is employed for transition metal atoms (Ni).³⁹ For all other main group elements (H, C, N, and O), the all-electron 6-31G* basis set^{40–42} was used. Harmonic vibrational frequencies were computed to make sure that all reaction intermediates have no imaginary frequency. The Gibbs free energies are calculated with the harmonic potential approximation at optimized structures at 298.15 K and 1 atm. Solvation free energies are calculated by the implicit SMD model⁴³ with M05-2X functional⁴⁴ and 6-31G* basis set, which is the level of theory where the SMD is parametrized against experimental data sets,⁴⁵ with water as the solvent.
148 149 150 151 152 153 154 155 156 157 158 159 160 161 162 163 164 165 166 167 168 169 170 171 172 173 174 175 176 177 178

MO analysis, generalized charge decomposition analysis, noncovalent interaction analysis, and electrostatic potential mapping are performed using Multiwfn on the previously obtained wave functions from DFT calculation.⁴⁶ Symmetry-adapted perturbation theory (SAPT)⁴⁷ calculations with restricted open-shell Hartree Fock (ROHF) reference are performed using PSI4 package⁴⁸ to decompose the interaction between the two fragments into components of physical meaning. For a better description of weak interactions while reducing the computational cost, the aug-cc-pVDZ basis set is used for Ni, the cc-pVDZ basis set is used for H, and the junc-cc-pVDZ basis set is used for all other elements.⁴⁹

The geometric optimization, adsorption energy, and charge density of NiPc molecules supported on nanocarbon substrate

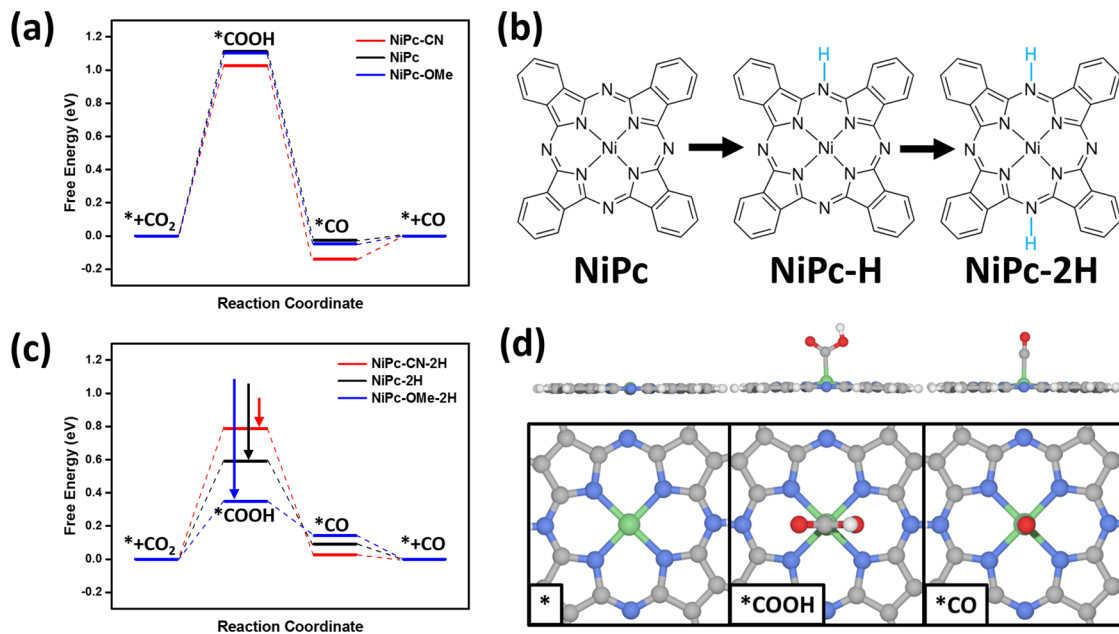


Figure 1. (a) Reaction profile of CO_2RR on NiPc, NiPc-CN, and NiPc-OMe. (b) Reductive activation process of NiPc. (c) Reaction profile of CO_2RR on NiPc-2H, NiPc-CN-2H, and NiPc-OMe-2H. (d) Optimized geometries of the three reaction intermediates, *, *COOH, and *CO, of CO_2RR on NiPc from top and side view. Color code: H, white; C, gray; N, blue; O, red; Ni, green.

are computed using the CP2K simulation package for its capability of efficiently computing relatively large systems (~ 400 atoms in this case).⁵⁰ The spin-polarized PBE exchange-correlation functional was adopted with double- ζ Gaussian basis sets for describing the valence electrons⁵¹ and an auxiliary plane-wave basis set with a cutoff of 400 Ry for computing the electrostatic terms.⁵² D3 correction is included to better describe the dispersion interaction. The nanocarbon substrate was modeled by a 12×12 graphene monolayer on which the NiPc molecule was placed in a face-to-face manner. A vacuum slab with thickness of 20 Å was added to eliminate the fictitious interaction in the Z-direction. Although the electronic structure of our employed model may deviate from that of CNT, a 1:1 model would otherwise be too computationally demanding (>2200 atoms for a 2 nm long fragment of CNT with 3 nm radius).⁵³ A model of CNT with a size reduced to affordable range or a bent graphene would cause more severe errors than this study due to a too-small curvature or spurious interactions.⁵⁴ In addition, the $\pi-\pi$ stacking energy has been shown to rely more on proper formulation of the dispersion term and the geometry than exact description of the band structures.⁵⁵ Hence, the main conclusions obtained with our model could translate to graphene, pyrolyzed graphitic carbon, and the outer wall of CNTs with small curvature.

SQM calculations are performed using the xTB package.⁵⁶ The GFN2-xTB tight binding method is employed in this study for its low computational cost on large systems and accuracy comparable to that of DFT methods in geometry optimization, noncovalent interaction, and MO energy calculation.⁵⁷ Since periodic GFN2-xTB is not yet implemented, the nanocarbon substrate is modeled by a 8×8 hexagonal graphene molecule cut out from monolayer graphene with terminal C atoms saturated with hydrogen.

In the computational screening section, each molecule is represented by a 1D vector with 42 (number of substituents) \times 8 (number of substitution sites) binary elements via positional

one-hot encoding. The representation can reversibly inter-
convert into or from a SMILES representation.⁵⁸ The SMILES string is converted to XYZ coordinates using Open Babel package,⁵⁹ and a sufficient stochastic conformational search is performed at the MMFF94 level to obtain the most stable conformation.⁶⁰

In the genetic algorithm search, each one-hot-encoded representation acts as a gene. On the basis of the calculated descriptors, a fitness factor is assigned to each candidate. Mating rates are assigned according to the fitness, and the child randomly inherits 50% of the gene from each of its parents. Mutations are introduced by choosing a substitution site and replacing the substituent on it randomly. The mutation rate is set at 33% to ensure sufficient sampling of the chemical subspace and to avoid being trapped into a local minima. When the population size exceeds the limit of 100 candidates, the candidates with the lowest fitness are removed. A GA run is regarded as converged when the fittest candidate remains in the pool for 50 generations.

The machine learning model for the fast prediction of molecular properties is a deep neural network (NN) with four rectified linear unit (ReLU)-activated hidden linear layers. The NN is trained on the data set of randomly sampled substituted NiPc, with 80% of the data as the training set and 20% of the data as the test set. Data augmentation is achieved by rotating the molecule to generate four equivalent representations for each data point. The validity of the machine learning model on the subspace that the current population is located is evaluated every 10 generations by calculating the R^2 between the NN-predicted value and the QM value. The NN is employed until the R^2 value drops below 0.9, after which the level of theory is switched to SQM methods in the subsequent generations.

■ RESULT AND DISCUSSION

CO_2 Electroreduction on NiPc Molecules with Different Substitutes. Previous experimental reports have shown that the NiPc molecule needs to go through two reduction

254 steps before it can catalyze the CO₂RR, as evidenced by the
255 two reduction peaks prior to the reduction current in
256 cyclovoltammetry, in the cases of both free-standing NiPc
257 and NiPc/CNT hybrids.^{32,61} Such a finding makes the
258 mechanistic studies based on the neutral NiPc molecule
259 problematic since the electronic structure of the Ni center can
260 change greatly after the reduction process. In addition, since
261 the standard reduction potential of the CO₂RR to CO (-0.10 V vs RHE in water) is more positive than the reduction
262 potential of NiPc molecule, the onset potential of the reaction
263 is likely to be dependent on the reductive activation of the
264 NiPc itself instead of the barriers of the electrocatalytic
265 process. For example, the energy profile of the CO₂RR on
266 neutral NiPc calculated under the computational electrode
267 (CHE) scheme and with implicit solvation model predicts a
268 prohibitively high overpotential of over 1.1 V (Figure 1a),
269 which deviates from experimental values greatly. It is hence
270 crucial to resolve the entity of the NiPc after reductive
271 activation. There are earlier reports proposing the stepwise
272 NiPc \rightarrow [NiPc]⁻ \rightarrow [NiPc]²⁻ mechanism; however, it is
273 unlikely because the reductive activation is also observed on
274 NiPc/CNT, in which case negatively charged cathode would
275 naturally repel the NiPc away if it were reduced to anion,
276 which contradicts the absence of Ni content in the electrolyte
277 after electrolysis by ICP-MS, as shown in ref 32. Therefore, all
278 intermediate forms of NiPc should have zero net charge. In
279 addition, the N atoms bridging between the isoindole units in
280 NiPc gain an ~ 3 times larger negative charge compared to the
281 Ni center, assuming that it gains an extra electron to form
282 [NiPc]⁻ (Figure S1a,b), making the N sites easily subject to
283 protonation in the neutral aqueous media. In our recent work,
284 we combined DFT calculation and operando XAS to reveal the
285 molecular structure of the intermediate structures (Figure
286 1b).³² The reduction of NiPc is in fact coupled with the
287 protonation of the Pc ligand, and two such protonation steps
288 are needed to activate NiPc into the NiPc-2H species for the
289 CO₂RR. The free energy change for attaching H to the Pc
290 ligand has been calculated to be 0.32 , 0.54 , and 0.49 eV on
291 NiPc-CN, NiPc-OMe, and unsubstituted NiPc, respectively.
292 EWG can lower the protonation energy by depleting the
293 electron density over the ligand and lowering the LUMO
294 energy level to facilitate the reduction of the Pc ligand that
295 precedes the protonation, while the EDG does the opposite
296 job. This trend is consistent with the experimental reduction
297 potential and the calculated LUMO energy levels with R^2
298 values of 0.9896 and 0.9944 , respectively. The operando
299 XANES showed the gradual distortion and decomposition of
300 the Ni-N₄ unit due to Ni loss in the unstable NiPc@CNT and
301 NiPc-CN@CNT catalysts, which contradicts the formation
302 and repelling of [NiPc]²⁻ species which would instead result in
303 a fading pattern without distortion. The operando EXAFS
304 result is also consistent with the fitting based on the DFT-
305 optimized NiPc-2H geometry, featuring two different Ni-C
306 patterns (changing symmetry from D_{4v} to D_{2v} upon
307 protonation), and the same goes for the adsorbate config-
308 uration *CO. The energy profile of the CO₂RR is recalculated
309 on the protonated forms under the CHE scheme, and the
310 predicted overpotential is reduced to 0.59 V. Although the
311 overpotential of the CO₂RR calculated from CHE is not a
312 good indicator of actual reactivity since the onset is limited by
313 the reduction activation of NiPc, it still suggests the radical
314 change of electronic structure and energetics on NiPc-2H since
315 the geometries of *CO and *COOH on NiPc-2H (Figure 1d)

316 do not differ much from those on neutral NiPc. It should be
317 noted that the CHE calculation on the gas-phase geometry
318 with implicit solvation is a crude approximation to the physical
319 reality where the carbon substrate and explicitly water
320 molecules can play some role in modulating the electronic
321 structure of the molecule and stabilization of the reaction
322 intermediates.⁶²

323 To evaluate the effect on the NiPc by introducing
324 substituents, we further calculated the NiPc with tetramethoxy
325 substitution and with octacyano substitution, denoted as NiPc-
326 OMe and NiPc-CN, respectively. The -OMe and -CN
327 substituents are chosen for the availability of experimental data
328 and because they are the strongest EDG and EWG,
329 respectively. Little deviation from the geometries of
330 intermediates on neutral forms is observed, evidencing the
331 consistent reaction pathway of the three NiPc molecules. The
332 HOMO (highest occupied molecular orbital), LUMO (lowest
333 unoccupied molecular orbital), LUMO+1 (LUMO and
334 LUMO+1 are degenerate MOs), and LUMO+2, together
335 with their energy levels are summarized in Figure S2. It is
336 apparent that the HOMO and LUMO are mainly attributed to
337 the ligand, and a more rigorous orbital composition analysis
338 reveals the contribution of Ni to be $\sim 0\%$ for HOMO and $\sim 1\%$
339 for LUMO, indicating Pc as the redox center. The ligand-
340 centered redox chemistry is consistent with previous operando
341 XANES report where the oxidation state of Ni (+II) is almost
342 unchanged when the potential is increased from open-circuit
343 voltage to the potential of stable operation.³² It is also
344 supported by the electron density map in Figure S1a where the
345 absolute majority of the extra electron are located on the ligand
346 and that there is only a minor decrease in Ni Mulliken charge
347 by ~ 0.02 and a minor weakening of Ni-N Mayer bond order
348 by ~ 0.05 upon the formation of the NiPc-2H species.
349 Introduction of an EDG upshifts the MO energy levels,
350 making it harder to reduce, while an EWG would do the
351 opposite. By comparing the LUMO energies with experimental
352 reduction potential of the second activation steps (-0.22 V for
353 NiPc-CN, -0.64 V for NiPc, and -0.69 V for NiPc-OMe),³² it
354 is obvious that a lower LUMO energy leads to a less negative
355 reduction potential for activation, hence an earlier onset.
356 Furthermore, there exists a linear correlation between the
357 reduction potential and LUMO energy level with an R^2 value
358 of 0.9993 (Figure S3), which is consistent with the linear
359 relationships between DFT-calculated MO energy and redox
360 potential that have been reported on similar molecular
361 systems.⁶³⁻⁶⁵ Therefore, the LUMO energy level could act
362 as a decent descriptor for predicting the reduction potential of
363 the activation process. The LUMO+2 is an antibonding orbital
364 for all four Ni-N bonds in the Ni-N₄ moiety, the filling of
365 which at a high overpotential is likely to substantially weaken
366 the Ni-N bonds and lead to structural distortion and even
367 Ni-N cleavage. Therefore, from a MO perspective, introduc-
368 tion of an EDG does help prevent the breakage of the Ni-N₄
369 moiety by upshifting the energy level of antibonding LUMO+2
370 out of reach.

371 For the neutral NiPc species, the CO₂RR exhibits no
372 pronounced difference in energetics among the three
373 molecules (Figure 1a). However, in their activated form, the
374 energetics of the reaction intermediates on three molecules
375 differ. It can be seen in Figure 1c that the energy of *COOH is
376 in the order of NiPc-CN-2H > NiPc-2H > NiPc-OMe-2H,
377 while the energy of *CO is in the order of NiPc-OMe-2H >
378 NiPc-2H > NiPc-CN-2H. Despite the fact that the electro-
379

380 chemical barriers are not well described under the CHE
 381 scheme due to dependence of onset on reduction of the NiPc
 382 itself, the energy difference between intermediates on different
 383 molecules are worthy of discussion, since ΔG (change in Gibbs
 384 free energy) is not as reliable a metric as $\Delta\Delta G$ (change in ΔG
 385 upon changing substituents), especially for the thermodynamic
 386 CO desorption process. The $^*\text{CO}$ adsorption strength is
 387 calculated to be NiPc-CN > NiPc > NiPc-OMe, which
 388 contradicts with the conventional view that a more electron-
 389 rich center should bind CO more strongly due to enhanced
 390 back-donation. In contrast, the orbital interaction diagram
 391 from generalized charge decomposition analysis (GCDA)
 392 shows that there is no back-donation in the NiPc-2H*CO
 393 intermediate (Figure 2a). The π and π^* orbitals of CO have

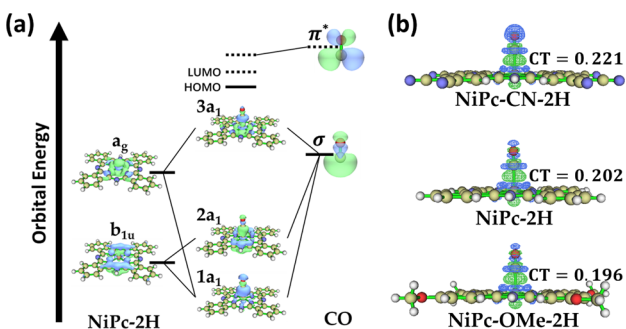


Figure 2. (a) Orbital interaction diagram of CO interacting with NiPc-2H from generalized charge decomposition analysis. Orbitals irrelevant with Ni–CO binding or having an insignificant contribution from CO are not shown for clarity. (b) Electron density difference plot at isovalue = 0.001 showing electron transfer from CO to NiPc-CN-2H, NiPc-2H, and NiPc-OMe-2H, with green and blue lobes showing increase and decrease of electron density, respectively. Integrated charge transfer obtained from generalized charge decomposition analysis are labeled next to the corresponding structural models. Color code: H, white; C, tan; N, blue; O, red; Ni, green.

394 little interaction with NiPc-2H MOs, and the CO π^* orbital is
 395 two MOs beyond the LUMO of NiPc-2H*CO, eliminating the
 396 presence of back-donation from the Ni d orbital to the CO π^*
 397 orbital. The adsorption of CO on Ni in NiPc-2H*CO is
 398 therefore mainly attributed to the CO σ orbital. As can be seen
 399 in Figure 2a, the σ orbital of CO interacts with the metal-
 400 centered MO a_g and the ligand-centered MO b_{1u} of NiPc-2H
 401 to form MO $1a_1$, $2a_1$, and $3a_1$ in the NiPc-2H*CO complex.
 402 MO $1a_1$, $2a_1$, and $3a_1$ are all occupied and far below the frontier
 403 orbitals. In terms of the Ni–C bond by σ -donation of CO to
 404 Ni, two of the three orbitals are bonding orbitals, while one is

405 antibonding. The Mayer bond order of Ni–C is calculated to
 406 be 0.52, which is significantly lower than the typical Ni–C
 407 coordination bond by σ -donation (the Ni–C in $\text{Ni}(\text{CO})_4$ has a
 408 Mayer bond order of 1.03).

The electron transfer from CO to Ni is visualized by the
 409 electron density difference map between the fragments (NiPc-
 410 2H and CO) and the complex (NiPc-2H*CO). From Figure
 411 2b, we found that the electron density shifts from O to C,
 412 forming the Ni–C bond through σ -donation. The injected
 413 electron density from CO mostly goes into the d_z^2 orbital,
 414 while the electron density at the Ni–N bond region is reduced
 415 caused by structural distortion and polarization, leading to
 416 weakening of the Ni–N bond as evidenced by the decrease of
 417 the Mayer bond order from 0.56 in NiPc-2H to 0.46 in NiPc-
 418 2H*CO. The electron transfer number from CO to Ni–N₄
 419 calculated by GCDA, as labeled below the electron density
 420 difference plot in Figure 2b, are 0.22, 0.20, and 0.19 lel for
 421 NiPc-CN-2H, NiPc-2H, and NiPc-OMe-2H, respectively. The
 422 smaller the electron transfer number, the weaker the
 423 interaction between the two fragments. The relationship can
 424 explain well the sequence of CO desorption energy: NiPc-CN-
 425 2H > NiPc-2H > NiPc-OMe-2H. The adsorption energy trend
 426 and Ni–N weakening upon CO adsorption also provides
 427 evidence for the experimental long-term stability of NiPc-OMe
 428 > NiPc > NiPc-CN, since the deactivation is mainly caused by
 429 poisoning of the active site by CO and loss of the Ni from Ni–
 430 N₄ breakage.

Having evaluated the bonding interactions, we further
 432 analyzed the noncovalent interactions (NCI) involved in the
 433 NiPc-2H and its $^*\text{COOH}$ and $^*\text{CO}$ intermediates. Figure 3
 434 shows the reduced density gradient (RDG) plot of NiPc-
 435 2H*CO and NiPc-2H*COOH. In Figure 3a, four red spikes
 436 can be observed between C in CO and the four N in Ni–N₄
 437 moiety, which correspond to the repulsive noncovalent
 438 interaction arising from the nonbonded overlap of electron
 439 density of C and the conjugate system over the Ni–N₄ moiety.
 440 Therefore, a more electron-rich Ni center would weaken the
 441 adsorption of CO. In Figure 3b, besides the similar red surfaces
 442 between C and Ni, the green RDG surfaces can be observed
 443 between the two O in $^*\text{COOH}$ and the center of the
 444 protonated ring in the Pc ligand, which suggests a slightly
 445 attractive van der Waals interaction. It is also worth noting that
 446 the protonated N–H moiety in NiPc-2H can be stabilized by
 447 the two beta C–H through a moderately attractive van der
 448 Waals interaction (Figure 3c). In addition, the steric bulk of
 449 the nearby isoindole units could also prevent the N–H from
 450 getting deprotonated by solvent molecules under weak
 451 oxidative potentials. For NiPc with a smaller electron density
 452 over the ring (by EWG functionalization), such a stabilization

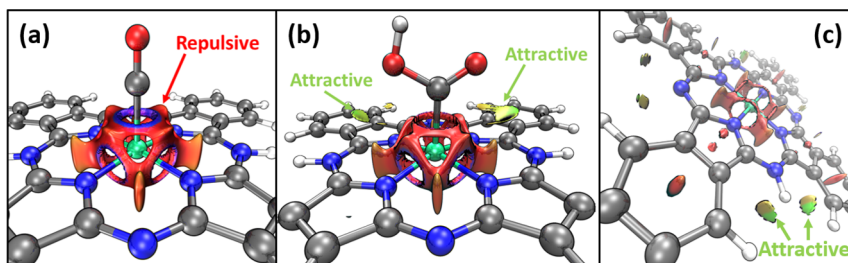


Figure 3. Reduced density gradient isosurfaces showing noncovalent interaction in (a) NiPc-2H*CO, (b) NiPc-2H*COOH, and (c) NiPc-2H. Red and green regions on isosurfaces correspond to repulsive and attractive noncovalent interactions, respectively. Color code: H, white; C, gray; N, blue; O, red; Ni, green.

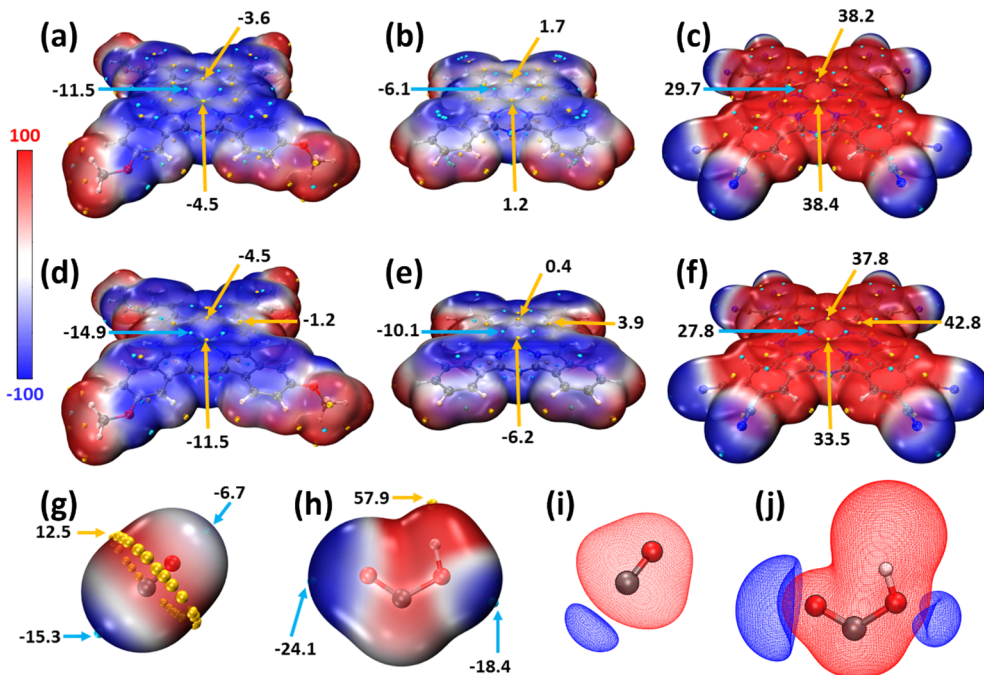


Figure 4. Electrostatic potential mapped van der Waals surface of (a) NiPc-CN, (b) NiPc, (c) NiPc-OMe, (d) NiPc-CN-2H, (e) NiPc-2H, (f) NiPc-OMe-2H, (g) CO fragment, and (h) COOH fragment. The electrostatic potential isosurfaces at 0.025 a.u. of (i) CO and (j) COOH fragments. Red and blue regions represent positive or negative electrostatic potential. Minima and maxima points are drawn as cyan and orange spheres, respectively. Unit of all labeled electrostatic potential values are kcal/mol. Color code: H, white; C, gray; N, blue; O, red; Ni, green.

effect would be weaker. This could explain why the CV of NiPc-CN@CNT is somewhat reversible, while that of NiPc-OMe@CNT is not in ref 32.

Since the weak interactions are shown to be present and may play a crucial role in the energetics of *CO and *COOH intermediates by NCI analysis, we calculated the electrostatic potential (ESP) of NiPc-OMe, NiPc, NiPc-CN (Figure 4a–c), and their activated species (Figure 4d–f) and mapped the ESP on their van der Waals surface. The ESP on Ni–N₄ moieties of all molecules share the same shape: one maximum above the Ni center, four minima above each of the four N atoms, and four maxima above each of the center of the 6-member rings. The EDG and EWG result in a more negative or a more positive ESP at the Ni–N₄ moiety, respectively. After the reductively activation, the maxima at Ni and minima at N of all three molecules shifts to a more negative value. The substituent effect still holds in the activated species. It is worth noting that the protonation breaks the D_{4h} symmetry of the electronic structure at Ni–N₄ moiety, leading to a relatively more positive ESP over the center of the protonated ring. To study the interaction between the activated molecules and the adsorbates, we also calculated the ESP of CO and COOH fragments. Figure 4g shows that the ESP minima on the CO surface lies at the C side, while the plane that intercepts the C=O has positive ESP. The ESP isosurfaces of CO (Figure 4i) indicate the presence of a lone pair at the C side, which supports the σ-donation bonding mode in Ni–N and causes the repulsion between C in CO and N in Ni–N. As for the COOH fragment, two ESP minima are located near the two O atoms and the H terminal of the –OH has an ESP maximum (Figure 4h). The ESP isosurfaces of COOH fragment reveal that the two ESP minima arise from the lone pairs of O atoms, and their docking with the relatively positive maxima on protonated ring of activated NiPc molecules likely give rise to

the attractive van der Waals interaction shown in Figure 3b. The C side at which COOH binds Ni, however, has positive ESP. In summary, the C sites in the CO and COOH fragments have different ESP, resulting in different energy trends when bound to the Ni–N₄ moiety.

To gain more detailed insights into the complex interaction between Ni–N₄ and adsorbent (CO and COOH), symmetry-adapted perturbation theory (SAPT) calculations with restricted open-shell Hartree Fock (ROHF) reference are performed to decompose the interaction between the two fragments into components of physical meaning. The decomposed energy components, together with the total SAPT energy, are summarized in Table 1. The total SAPT energy of *CO intermediates follows the sequence NiPc-CN-2H*CO < NiPc-2H*CO < NiPc-OMe-2H*CO, which is consistent with the DFT calculation. It can be seen that the interaction between Ni–N₄ and CO is dominated by repulsive exchange interaction, i.e., Pauli repulsion, between CO σ

Table 1. SAPT Energy Decomposition Results on NiPc-2H*CO, NiPc-CN-2H*CO, NiPc-OMe-2H*CO, NiPc-2H*COOH, NiPc-CN-2H*COOH, and NiPc-OMe-2H*COOH^a

	E _{electrostat}	E _{exchange}	E _{induction}	E _{dispersion}	E _{SAPT}
NiPc-CN-2H*CO	-51.89	83.59	-13.18	-12.65	5.87
NiPc-2H*CO	-55.17	88.26	-12.91	-13.03	7.16
NiPc-OMe-2H*CO	-55.65	88.96	-13.00	-13.11	7.20
NiPc-CN-2H*COOH	-35.52	79.12	-11.74	-18.87	12.99
NiPc-2H*COOH	-36.82	78.27	-21.65	-18.55	1.25
NiPc-OMe-2H*COOH	-36.73	78.06	-24.42	-18.54	-1.63

^aAll units are kcal/mol.

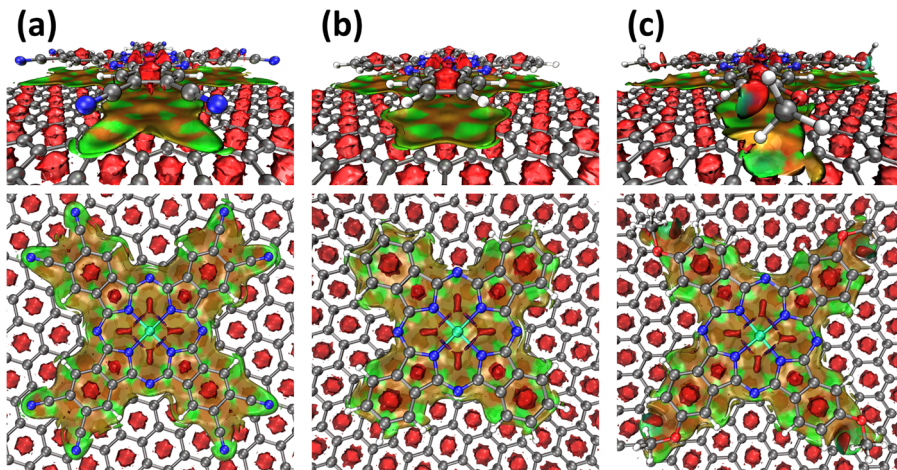


Figure 5. Reduced density gradient isosurfaces from promolecular density showing noncovalent interaction at the interface of (a) NiPc-CN@NC, (b) NiPc@NC, and (c) NiPc-OMe@NC. Red and green regions on isosurfaces correspond to repulsive and attractive noncovalent interactions, respectively. Color code: H, white; C, gray; N, blue; O, red; Ni, green.

506 orbital and the π orbital over the electron-rich Ni–N₄ region
 507 after reduction as evidenced in Figure 3a. However, in the case
 508 of *COOH, the pronounced difference of induction energy
 509 among the three species makes induction energy the
 510 dominating contributor to the difference between three
 511 substituted NiPc molecules. Due to the positive atomic charge
 512 of C in COOH as evidenced in Figure 4j, a more electron-rich
 513 Ni center would result in a stronger induction interaction
 514 between Ni and C in *COOH. This can be also supported by
 515 the atomic charge calculated by modified Mulliken atom
 516 population defined by Bickelhaupt, which is 0.92, 0.87, and
 517 0.86 for NiPc-CN-2H, NiPc-2H, and NiPc-OMe-2H,
 518 respectively. Therefore, when an EDG is introduced to the
 519 NiPc, the Ni–N₄ moiety becomes more electron-rich, resulting
 520 in strengthened COOH binding and weakened CO binding.
 521

Molecular Catalyst/Support Interaction. The diverse
 522 adsorption properties induced by molecular engineering
 523 inspires us to look further into other factors that may be in
 524 effect in the realistic electrocatalytic system. Although the
 525 supported NiPc on nanocarbon (NC) substrate can preserve
 526 its structure and well-defined Ni–N₄ center, the interaction
 527 between NiPc molecules and NC could vary for different
 528 substituents. In operation, the electrons driven by applied
 529 potential move from electrode to NC and then transfer to the
 530 supported NiPc molecule via through-space electron transfer
 531 across the π – π stacking interface. In addition, strong enough
 532 π – π stacking interaction is a prerequisite of the hybrid system
 533 since NiPc needs to be immobilized on the NC in a stable way.
 534 Therefore, the molecular catalyst/support interaction is worth
 535 exploration.

536 In the DFT calculation, the NC substrate is modeled a
 537 sufficiently large periodic graphene monolayer. Due to the
 538 relatively large radius of CNT (20–30 nm) compared to the
 539 size of the NiPc molecule (<1 nm), the curvature of the
 540 graphitic carbon layer at the interface is negligible. Therefore,
 541 the graphene monolayer model can also act as an affordable
 542 approximation to the CNT surface. The geometries are
 543 optimized at PBE-D3 with double- ζ Gaussian-planewave
 544 basis set to obtain the π – π stacking geometry.

545 The adsorption energies (E_{ads}) of NiPc, NiPc-CN, and
 546 NiPc-OMe on graphene are calculated to evaluate the strength
 547 of interaction between them. The E_{ads} are -2.47, -2.88, and

-3.52 eV for NiPc, NiPc-OMe, and NiPc-CN, respectively. 548 The strengths of adsorption are in order NiPc-CN > NiPc- 549 OMe > NiPc, which surprisingly does not fit into the the 550 EDG/EWG-tuning context which would predict either NiPc- 551 OMe > NiPc > NiPc-CN or NiPc-CN > NiPc > NiPc-OMe. 552 To gain a deeper understanding of the interaction, NCI 553 analysis is performed on the three hybrid structures to visualize 554 the noncovalent interaction between the graphene and NiPc 555 molecules (Figure 5). All three NiPc molecules are about 3.2 Å 556 fs from the graphene surface, and the RDG surface at the 557 interface in between is colored in a mixture of green and 558 brown, suggesting the nature of π – π stacking to be mainly 559 attractive van der Waals interaction. The surface between the 560 main body of the Pc ligand and the graphene are very similar 561 among the three hybrids, however, the regions below the 562 substituents differ greatly. The terminal H at the pristine NiPc 563 has little interaction with the graphene (Figure 5b); however, 564 the cyano groups in NiPc-CN (Figure 5a) and methoxy groups 565 in NiPc-OMe (Figure 5c) extend the RDG surface, 566 representing an additional attractive contribution. Therefore, 567 the π – π stacking is not directly reliant on the electron push– 568 pull effects of the substituents but depends more on the 569 polarizability of the substituent fragment (for enhanced 570 dispersion interaction) and whether the substituent contains 571 pi MOs to extend the conjugated system of the Pc ligand (for 572 expanded interaction region). From the previously calculated 573 ESP map in Figure 4, it can be seen that the charge 574 redistribution is much more pronounced (evidenced by more 575 extreme ESP values) on NiPc-CN and NiPc-OMe compared 576 to NiPc. The dependence of π – π stacking strength on nature 577 of the substituents is consistent with previous reports on 578 substituted aromatic molecules.⁶⁶ 579

Since the interaction between NiPc molecules and graphene 580 is pure π – π stacking without any chemical bond, a stronger 581 interaction between them should give rise to stronger coupling 582 of the electronic structure and hence facilitate electron transfer 583 and transport, which is of grave importance in the electro- 584 catalytic process but is often neglected in computational 585 studies. Here we apply a surface charging technique to 586 investigate the effect of substituents on the electron transfer at 587 the interface. To be specific, one additional electron is added 588 to the graphene to model the negatively charged NC surface, 589

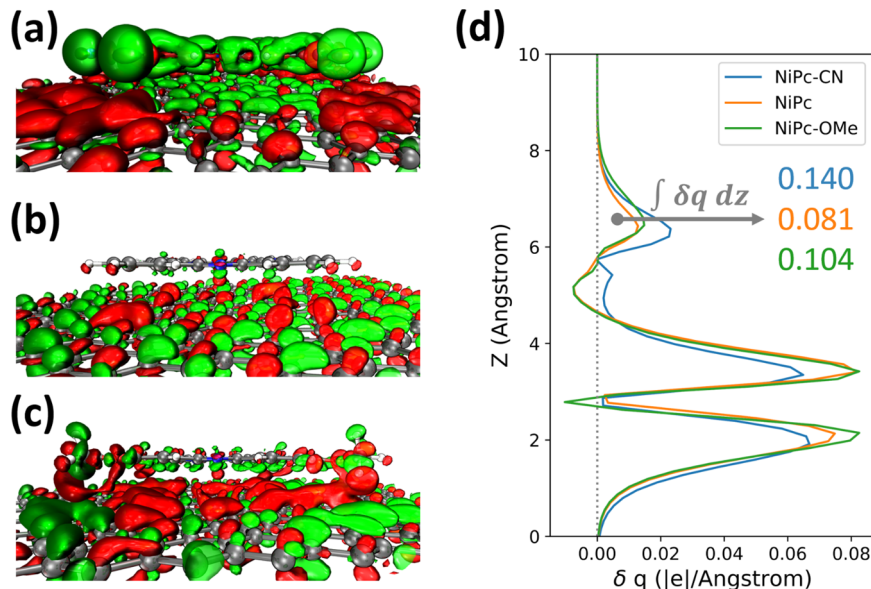


Figure 6. Electron density difference plot (isovalue = 0.0025) showing charge transfer from a negatively charged graphene substrate to adsorbed (a) NiPc-CN, (b) NiPc, and (c) NiPc-OMe on graphene substrate. Green and red isosurfaces show increase or decrease of electron density, respectively. (d) Electron density difference after surface charging, projected to the Z-direction. The number of electrons gained by NiPc molecules from surface charging is calculated by integrating the charge density difference over the region around NiPc molecules, and the values are labeled in the plot.

and the neutral NiPc molecule is attached to the charged surface. The negatively charged hybrid is relaxed to its local minimum. By subtracting the electron density of the charged graphene substrate and the neutral NiPc from the charged hybrid, the electron transfer to NiPc can be visualized by the electron density difference map. Since the number of extra electrons added to the graphene substrate is the same among the three hybrids, the driving force for electron transfer should be the same. However, the charge transfer behavior is quite different among the three hybrids. In Figure 6b, polarization of the graphene substrate can be observed, but the isosurfaces on the NiPc molecule are so tiny that the charge transfer through the interface is almost negligible. In Figure 6a, we can see enhanced polarization of NiPc-CN and the graphene substrate, and the green isosurfaces corresponding to electron gain have a much larger size. NiPc-OMe does not have as large green isosurfaces as NiPc-CN, but they are more pronounced than those of the pristine NiPc molecule. The major charge transfer happens at the region between the substituent groups and the substrate as can be seen in Figure 6a,c, providing another evidence that the molecule/substrate interaction is substituent-dependent instead of the result of the electron push-pull effects.

To quantify the electron gain at the NiPc molecules from surface charging, we subtract the electron density of the neutral hybrid from the charged hybrid and project the electron density increases to the Z-direction (vertical to the graphene plane). Although a more sophisticated Poisson–Boltzmann model under the grand canonical DFT scheme, which would require a symmetrizing slab, polarizable continuum, and a much thicker vacuum, is not employed due to extremely high computational cost with our already large model, the resulting error would be ~ 100 meV and is systematic.⁶⁷ The Z-coordinate of graphene substrate is at 2.8 Å; therefore, the two large peaks of electron density above and below $Z = 2.8$ Å indicate that the majority of the extra electrons are injected

into the Π conjugate system of graphene. As the Z-value increases, the electron density declines to around zero across the through-space region and then goes up at the position of the NiPc molecules. Above the Z-position of zero flux at around 5.75 Å, the smaller peak at around $Z = 6.2$ Å corresponds to the electron that is successfully transferred to NiPc. By integrating the charge density across such region, the number of gained electrons is quantitatively calculated as 0.140, 0.081, and 0.104 e⁻ for NiPc-CN, NiPc, and NiPc-OMe, respectively, indicating the order of charge transfer ability was NiPc-CN@NC > NiPc-OMe@NC > NiPc@NC. Moreover, the charge transfer number correlates well with calculated adsorption energies linearly with an R^2 value of 0.9999 (Figure S4), establishing the adsorption energy of NiPc on substrate as a viable descriptor of charge transfer kinetics at the π – π stacking interface.

We would like to note that although vacuum model or implicit solvation model are used throughout the previous sections, we are fully aware of their limitations. From our primitive tests, including a microsolvation of 8 explicit water molecules around the periphery of the NiPc-2H could lead to charge transfer of -0.16 , -0.24 , and $+0.20$ from the water to the NiPc-2H molecules for unsubstituted, $-CN$, and $-OMe$, respectively (Figure S5). The electron density differs from the isolated case not only near the peripheral rings but also at the $Ni-N_4$ moiety, with the extent differing from substituent to substituent, thereby influencing the ground-state redox properties. It has recently been reported that including a full realistic explicit solvation layer could alter the reaction energetics by a few hundred meV via hydrogen bonding stabilization and could even reveal alternative reaction pathways.⁶⁸ We are currently working to incorporate the explicit solvent environments, together with the substrate part that we are to discuss in the next section, into a unified realistic model for electrocatalysis.

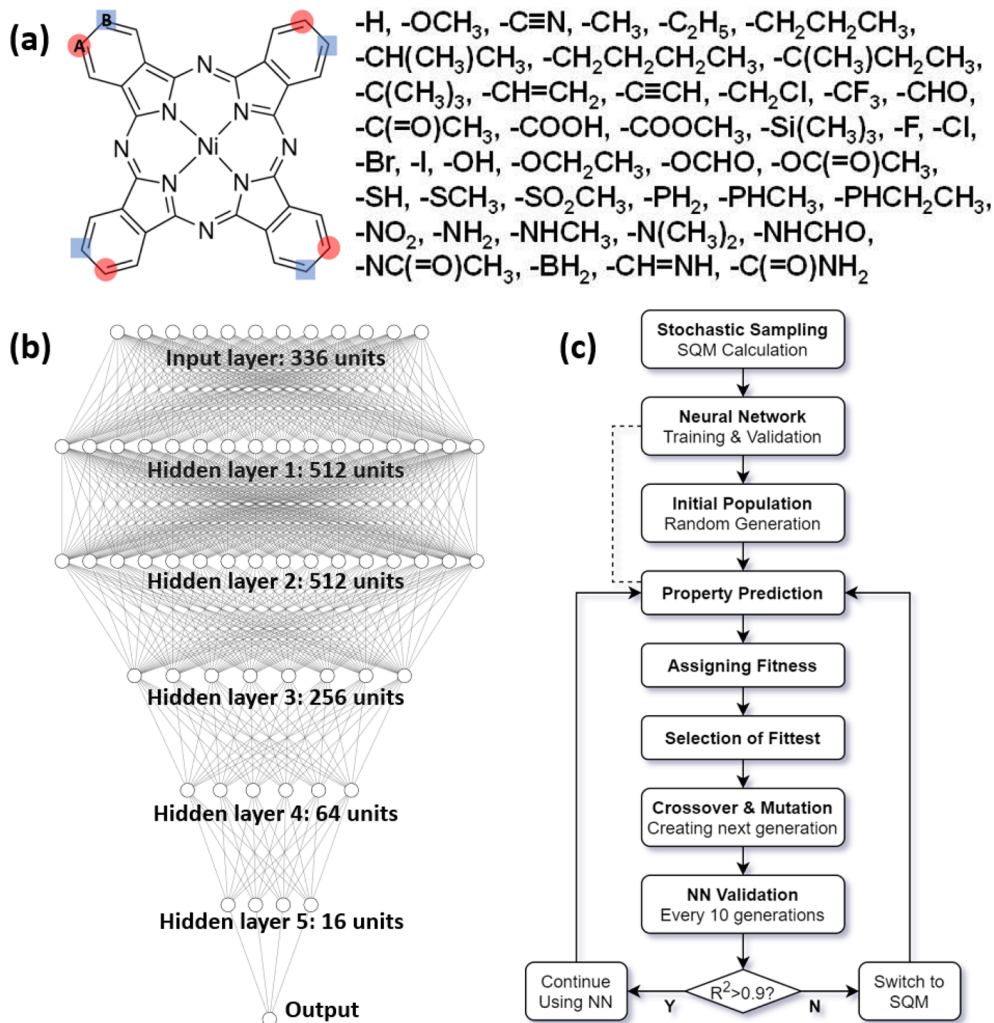


Figure 7. (a) Structural formula of the NiPc with blue square and red circles labeling the peripheral sites where substituents are introduced, denoted as site A and site B, respectively. The full list of substituent scope is provided on the right. (b) Architecture of the deep neural network for property prediction in this study. (c) General workflow of the genetic algorithm search.

661 **Computational Screening.** Sufficient insights into the
 662 substituent effects on the electronic structure of NiPc has been
 663 gained in the previous sections, and a few relationships are also
 664 discovered along the way: (i) The more electron-rich metal
 665 center weakens CO adsorption to prevent poisoning. (ii) The
 666 more electron-rich metal center strengthens the Ni–N bond to
 667 protect integrity of the Ni–N₄ moiety. (iii) A lower LUMO
 668 energy level makes the reduction potential for activation of the
 669 NiPc molecule less negative. (iv) A stronger interaction energy
 670 with substrate means charge transfer is facilitated across the
 671 interface and ensures the immobilization. Inspired by the
 672 findings, we expand the scope to 42 types of substituents, with
 673 the full list provided in Figure 7a. To deal with the vast number
 674 of molecular permutations to explore in this rather large
 675 chemical space, we employ the recently developed SQM
 676 method GFN2-xTB to perform all the calculations in this
 677 section. The method is grounded quantum mechanically and
 678 has been benchmarked to predict geometry and molecular
 679 properties of with comparable accuracy to DFT.⁵⁷ In our tests,
 680 the LUMO energy level calculated at GFN2-xTB linearly
 681 correlates well with the DFT result, with an R^2 value of 0.9999
 682 (Figure S6). The geometry and RDG surfaces of NiPc
 683 interacting with substrate calculated at GFN2-xTB (Figure

684 S7) are also consistent with the DFT results, proving that the
 685 NCI are correctly described. Although the substrate is modeled
 686 by a smaller aperiodic graphitic carbon sheet at GFN2-xTB
 687 instead of the periodic graphene model in previous DFT
 688 calculations, the interaction energy linearly correlates decently
 689 with an R^2 value of 0.9844 (Figure S8).

We begin with a data set of symmetrically tetra- and octasubstituted NiPc molecules, i.e., substituting site A or both sites A and B with the same substituent, with a total number of 83 molecules. The Mulliken charge of Ni atom, the Mayer bond order of Ni–N, and the LUMO and HOMO energy levels of each molecule in the library are calculated after geometric optimization by SQM. It can be seen from Figure 8a that the Mulliken charge of the Ni center is negatively correlated to the Mayer bond order of Ni–N, which echoes the previous finding that a more electron-rich Ni center strengthens the Ni–N bond. Therefore, the two aspects of long-term stability can be described by one variable, the Mulliken charge of the Ni center, to eliminate one degree of freedom. Since the atomic charge is related to the occupied orbitals, the HOMO energy level usually correlates with the atomic charge or oxidation state.⁶⁹ Unfortunately, on this symmetric data set, the HOMO and LUMO energy levels are

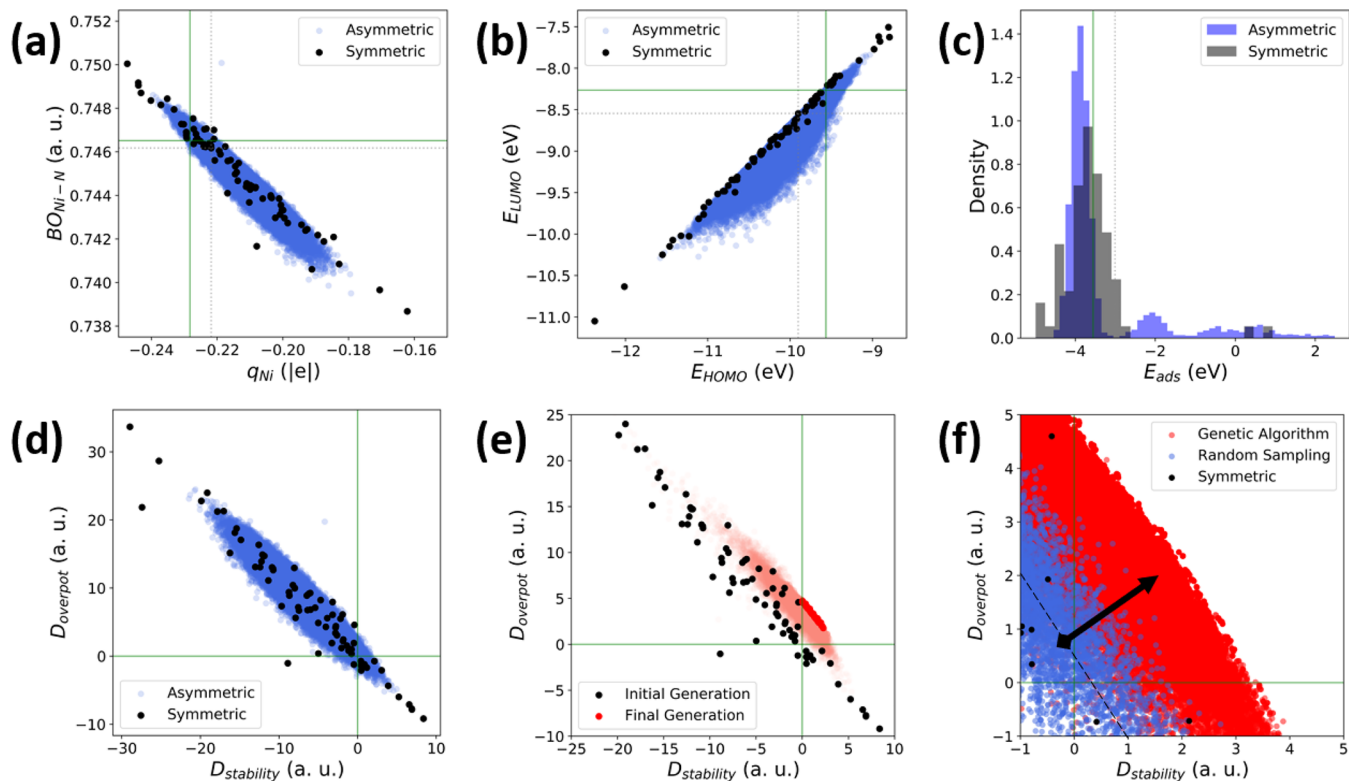


Figure 8. (a) Scatter plot of Mayer bond order of Ni–N versus atomic partial charge of Ni center of symmetrically and stochastically sampled asymmetrically substituted NiPc molecules. (b) Scatter plot of LUMO energy level versus HOMO energy level of symmetrically and stochastically sampled asymmetrically substituted NiPc molecules. (c) Histogram showing distribution of adsorption energies on graphene sheet of symmetrically and stochastically sampled asymmetrically substituted NiPc molecules. (d) Scatter plot of potential descriptor versus stability descriptor of symmetrically and stochastically sampled asymmetrically substituted NiPc molecules. (e) Scatter plot of potential descriptor versus stability descriptor on the trajectory of genetic algorithm search. (f) Scatter plot of potential descriptor versus stability descriptor of symmetrically and stochastically sampled asymmetrically substituted NiPc molecules, and trajectory of 10 independent GA searches. Gray dotted lines and green lines represent the values of NiPc and NiPc-OMe for reference. Dashed line and arrow in (f) represent the linear overpotential–stability correlation fitted on the stochastic data set and the normal search direction.

correlated. Since the LUMO energy level has been shown to correlate with the reduction potential, the molecular design comes to a dilemma where improving the stability would make the reduction potential more negative.

Recalling that MO analysis indicates degenerate LUMO and LUMO+1 on symmetrically substituted NiPc molecules (Figure S2), asymmetric substitution is introduced to break the degeneracy to lower the LUMO energy levels without making as significant changes to the HOMO energy levels. Since there are 42 different substituent including hydrogen and 8 substitution sites on NiPc, the chemical space would have size of ca. 10 trillion molecules ($\sim 42^8$) which is beyond the capability of any brute-force exhaustion. Hence, we adopt a stochastic sampling to randomly introduce substituents on to the NiPc without any restriction on symmetry of number of different substituents, with a total size of 100 000 distinct molecules. After introducing asymmetric substitution, the LUMO and HOMO can be decoupled to some extent (Figure 8b), thereby making some room for optimization of performance beyond the scaling relation. On the basis of the understandings and the previously obtained correlations between calculated property and experimental values, we define a descriptor-based scheme to evaluate the overall performance of the substituted NiPc molecule. The descriptor of reduction potential of activation, $D_{\text{potential}}$, is defined as

$$D_{\text{potential}}(X) = \frac{E_{\text{LUMO}}(\text{ref}) - E_{\text{LUMO}}(X)}{|E_{\text{LUMO}}(\text{ref})|} \times 100$$

The descriptor of long-term stability, $D_{\text{stability}}$, is defined as 732

$$D_{\text{stability}}(X) = \frac{q_{\text{Ni}}(X) - q_{\text{Ni}}(\text{ref})}{|q_{\text{Ni}}(\text{ref})|} \times 100$$

where the X is a substituted NiPc, the ref denotes the reference molecule, and E_{LUMO} and q_{Ni} are the LUMO energy level and Mulliken charge of the Ni center calculated by SQM, respectively. In this study, the reference molecule is chosen as NiPc-OMe since it is the highest performing molecule in the NiPc family that has been reported to date. The $D_{\text{potential}}$ is plotted versus $D_{\text{stability}}$ on the symmetric and asymmetric data set in Figure 8d. Despite the negative correlation between stability and potential, it is not a strict linear relationship. It is worth noting that in the symmetric data set no molecule that can outperform NiPc-OMe in both aspects (no black data points in first quartet), indicating it as the likely best candidate in this synthesis-friendly chemical subspace. On the asymmetric data set, there are 572 molecules outperforming the reference molecule in terms of both stability and in potential, which is only 0.57% of all samples. Despite the excitement of this result, one should be cautious since the asymmetric substitution can also lead to molecular structures that are sterically unfavorable for immobilization due to substituents

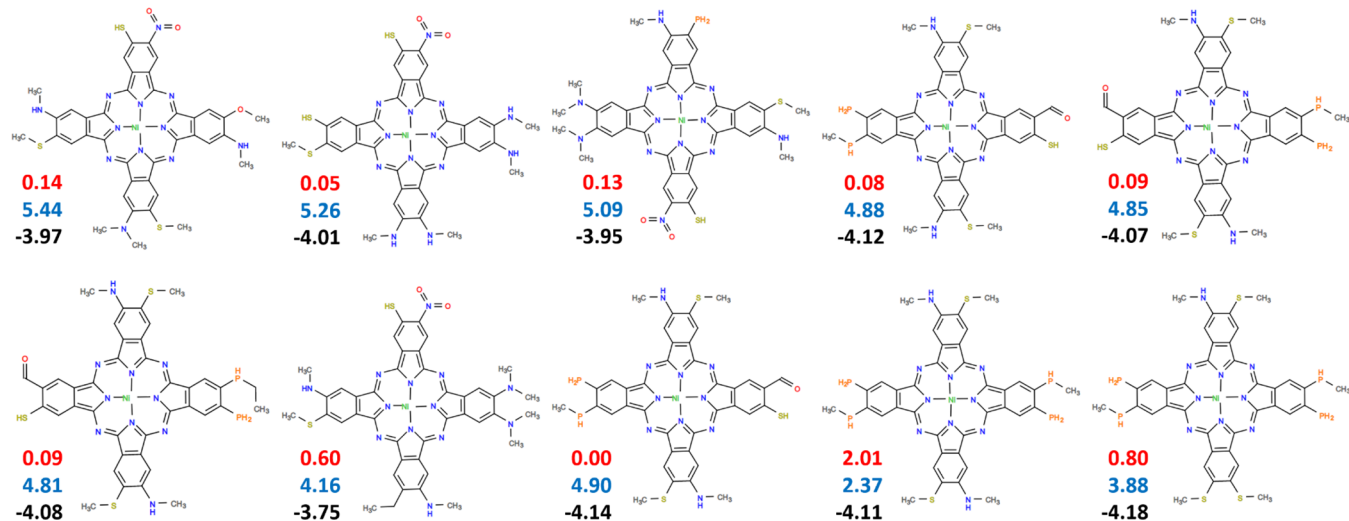


Figure 9. Structure of the top 10 substituted NiPc molecules with optimal performance from 10 independent genetic algorithm runs. The stability descriptor (top, in red), potential descriptor (middle, in blue), and adsorption energy on substrate in eV (bottom, in black) are labeled in the lower left of each molecule.

sticking out-of-plane from steric repulsions, as can be seen in the peaks with positive adsorption energy in Figure 8c. This demonstrates the necessity to take into account the interaction with substrate in molecular design.

The best-performing molecules from the stochastic sampling are definitely not the best in the whole chemical space of substituted NiPc since a data set of 10^4 molecules is just a drop of water in ocean of 10^{12} molecules. Stochastic sampling allows uniform exploration of the chemical space, but it is inefficient in optimizing toward a specific property. However, the sheer size of data set makes even semiempirical methods extremely expensive. To explore efficiently the vast chemical space of asymmetrically substituted NiPc in an affordable way, we develop a GA searcher for global optimization of NiPc properties in the chemical space of substituent permutations and integrate NN models into the search. The workflow of the GA searcher and the architecture of the NN are shown in Figure 7b,c, respectively. The NN is trained on the data-augmented stochastic sampled data set with the one-hot-encoded representation of the NiPc as input. The trained NN can achieve pretty accurate prediction of $D_{\text{potential}}$, $D_{\text{stability}}$, and E_{ads} on the test set with R^2 values of 0.9853, 0.9907, and 0.9990, respectively (Figure S9). Since the training set does not contain a sufficient sampling of the outliers, especially in the direction of GA search, the validity of the NN-predicted value is checked on-the-fly against the SQM level results every 10 generations. The property calculation method is switched back to SQM after the R^2 of the NN-predictions drops below 0.9, which indicates insufficient training of the NN model in this chemical subspace. Molecules with positive E_{ads} are removed in each generation to avoid misguiding the search direction. For the candidates with a negative E_{ads} , the projection of ($D_{\text{stability}}$, D_{overpot}) to the normal vector (arrow in Figure 8f) of the fitted $D_{\text{stability}} - D_{\text{overpot}}$ linear correlation (dashed line in Figure 8f) is calculated, and the maximization of which is set as the search direction. Ten GA searches are performed with a population size of 100, a mutation rate of 33%, and a convergence criterion of 50 generations. Figure 8e shows the results from one of the GA searches, and it can be seen that the population gradually evolves from the diverse but ill-performing initial generation to higher scoring populations

and that in the final population all the molecules outperform the reference molecules. The GA also has much improved efficiency from the stochastic search since the sampling of the ill-performing regions is avoided, with 42.90% of the sampled molecules outperforming reference molecules. In Figure 8f, we summarize the result from all 10 GA searches and zoom in at the region of improved performance. The resulting molecules from GA greatly outperform the ones from stochastic sampling by ~ 2 folds in $D_{\text{potential}}$ and by ~ 3 folds in $D_{\text{stability}}$. The final top 10 highest scoring molecules are shown in Figure 9. The best candidate has slightly improved long-term stability and a 0.46 eV stronger substrate interaction compared to the reference molecule. Its $D_{\text{potential}}$ is 5.44 which corresponds to a reduction potential of -0.59 V, which is 100 mV less negative than the state-of-the-art NiPc-OMe. To verify the GA search results, DFT calculations are performed on the 10 molecules at the same level of theory as in the previous section (Figure S10). All 10 molecules show less negative reduction potentials, with the best among them (no. 8) outperforming the reference molecule NiPc-OMe by 110 mV. In terms of stability, four of them (nos. 2 and 8–10) significantly outperform the reference molecule, while three of them (nos. 1, 5, and 6) show a small compromise in stability but still outperform the unsubstituted NiPc. In summary, 7 of the 10 top-scoring molecules from the GA search are promising candidates for CO_2 reduction reaction.

Some design strategies for NiPc can also be proposed based on the molecular structure of the search results: (i) introduce an EDG to improve long-term stability, (ii) include different types of substituents with distinct electron push–pull effects to break the degeneracy of LUMO/LUMO+1 for a less negative reduction potential, and (iii) introducing a small number of strong EWG can further break the degeneracy of LUMO and maximize the molecular polarizability for enhanced non-covalent interaction with substrate.

CONCLUSIONS

In summary, we studied the reaction mechanism of the CO_2 RR to CO on NiPc by DFT calculation, with an emphasis on the preceding reductive activation. The electronic structure and adsorption properties of the Ni–N₄ moiety, as well as how

they are affected by substituents, are investigated in detail by analyzing molecular orbitals, generalized charge decomposition, electron density difference map, reduced density gradient map, electrostatic potential map, and symmetry-adapted perturbation theory energy decomposition. The adsorption property and structural stability of the Ni–N₄ moiety is found to be related to electron density near the Ni center, making it readily tunable by attaching EWG and EDG. The interaction between NiPc and the nanocarbon substrate is also investigated, and a correlation is discovered between the interaction energy and the charge transfer across the π–π stacking interface. Such interaction strength is related to the polarizability of the molecule and the nature of the substituent instead of the electron push–pull effects on the Ni–N₄ moiety, opening up an additional dimension in molecular design. Finally, we developed a descriptor-based scheme for performance evaluation of the candidate molecule and screened through the chemical space of substituted NiPc using a genetic algorithm search with semiempirical quantum mechanical calculations and predictive deep neural network models. Several promising molecules are identified, with the best one outperforming the state-of-the-art reference molecule in stability and in reduction potential by 100 mV. Design strategies are proposed based on the top-down computational screening, and the workflow is highly generalizable and transferable to similar hybrid materials for various applications.

ASSOCIATED CONTENT

Supporting Information

The Supporting Information is available free of charge at <https://pubs.acs.org/doi/10.1021/acs.jpcc.1c02508>.

Electron density map and color-filled cross section of the electron density increment of NiPc after reduction; molecular orbital isosurfaces and energy levels of NiPc, NiPc-OMe, and NiPc-CN; correlation plots; reduced density gradient isosurfaces showing substrate interactions at GFN2-xTB; validation of the trained machine learning models ([PDF](#))

AUTHOR INFORMATION

Corresponding Author

Yang-Gang Wang – Department of Chemistry, Southern University of Science and Technology, Shenzhen 518055, China; orcid.org/0000-0002-0582-0855; Email: wangyg@sustech.edu.cn

Author

Zisheng Zhang – Department of Chemistry, Southern University of Science and Technology, Shenzhen 518055, China; Present Address: Department of Chemistry and Biochemistry, University of California, Los Angeles, 607 Charles E. Young Drive East, Los Angeles, CA 90095, United States; orcid.org/0000-0002-4370-4038

Complete contact information is available at:

<https://pubs.acs.org/10.1021/acs.jpcc.1c02508>

Notes

The authors declare no competing financial interest.
The scripts for running genetic algorithm and deep neural network fitting, and the trained model.pkl files are available on: <https://github.com/zishengz/molga-mpc>.

ACKNOWLEDGMENTS

This work was financially supported by NSFC (No. 22022504) of China, the Guangdong “Pearl River” Talent Plan (No. 2019QN01L353), the Higher Education Innovation Strong School Project of Guangdong Province of China (2020KTSCX122), and the Guangdong Provincial Key Laboratory of Catalysis (No. 2020B121201002). The computational resource is supported by the Center for Computational Science and Engineering at SUSTech.

REFERENCES

- (1) Froelicher, T. L.; Paynter, D. J. Extending the Relationship between Global Warming and Cumulative Carbon Emissions to Multi-Millennial Timescales. *Environ. Res. Lett.* **2015**, *10* (7), 075002.
- (2) Seh, Z. W.; Kibsgaard, J.; Dickens, C. F.; Chorkendorff, I. B.; Nørskov, J. K.; Jaramillo, T. F. Combining Theory and Experiment in Electrocatalysis: Insights into Materials Design. *Science (Washington, DC, U. S.)* **2017**, *355* (6321), No. eaad4998.
- (3) Zhang, W.; Hu, Y.; Ma, L.; Zhu, G.; Wang, Y.; Xue, X.; Chen, R.; Yang, S.; Jin, Z. Progress and Perspective of Electrocatalytic CO₂ Reduction for Renewable Carbonaceous Fuels and Chemicals. *Adv. Sci.* **2018**, *5* (1), 1700275.
- (4) Jones, J.; Prakash, G. K. S.; Olah, G. A. Electrochemical CO₂ Reduction: Recent Advances and Current Trends. *Isr. J. Chem.* **2014**, *54* (10), 1451–1466.
- (5) Yang, X.-F.; Wang, A.; Qiao, B.; Li, J.; Liu, J.; Zhang, T. Single-Atom Catalysts: A New Frontier in Heterogeneous Catalysis. *Acc. Chem. Res.* **2013**, *46* (8), 1740–1748.
- (6) Wang, A.; Li, J.; Zhang, T. Heterogeneous Single-Atom Catalysis. *Nat. Rev. Chem.* **2018**, *2*, 65–81.
- (7) Zhu, C.; Fu, S.; Shi, Q.; Du, D.; Lin, Y. Single-atom Electrocatalysts. *Angew. Chem., Int. Ed.* **2017**, *56* (45), 13944–13960.
- (8) Li, X.; Wang, H.; Yang, H.; Cai, W.; Liu, S.; Liu, B. In Situ/Operando Characterization Techniques to Probe the Electrochemical Reactions for Energy Conversion. *Small Methods* **2018**, *2* (6), 923 1700395.
- (9) Su, X.; Yang, X.-F.; Huang, Y.; Liu, B.; Zhang, T. Single-Atom Catalysis toward Efficient CO₂ Conversion to CO and Formate Products. *Acc. Chem. Res.* **2019**, *52* (3), 656–664.
- (10) Chen, Y.; Yu, G.; Chen, W.; Liu, Y.; Li, G.-D.; Zhu, P.; Tao, Q.; Li, Q.; Liu, J.; Shen, X.; Li, H.; Huang, X.; Wang, D.; Asefa, T.; Zou, X. Highly Active, Nonprecious Electrocatalyst Comprising Borophene Subunits for the Hydrogen Evolution Reaction. *J. Am. Chem. Soc.* **2017**, *139* (36), 12370–12373.
- (11) Yang, H. B.; Hung, S.-F.; Liu, S.; Yuan, K.; Miao, S.; Zhang, L.; Huang, X.; Wang, H.-Y.; Cai, W.; Chen, R.; et al. Atomically Dispersed Ni (I) as the Active Site for Electrochemical CO Reduction. *Nat. Energy* **2018**, *3* (2), 140–147.
- (12) Sun, T.; Xu, L.; Wang, D.; Li, Y. Metal Organic Frameworks Derived Single Atom Catalysts for Electrocatalytic Energy Conversion. *Nano Res.* **2019**, *12*, 2067–2080.
- (13) Lee, L. K.; Sabelli, N. H.; LeBreton, P. R. Theoretical Characterization of Phthalocyanine, Tetraazaporphyrin, Tetrabenzo-porphyrin, and Porphyrin Electronic Spectra. *J. Phys. Chem.* **1982**, *86* (20), 3926–3931.
- (14) Marom, N.; Kronik, L. Density Functional Theory of Transition Metal Phthalocyanines, I: Electronic Structure of NiPc and CoPc Self-Interaction Effects. *Appl. Phys. A: Mater. Sci. Process.* **2009**, *95* (1), 159–163.
- (15) Drexler, K. E. Molecular Engineering: An Approach to the Development of General Capabilities for Molecular Manipulation. *Proc. Natl. Acad. Sci. U. S. A.* **1981**, *78* (9), 5275–5278.
- (16) Solis, B. H.; Hammes-Schiffer, S. Proton-Coupled Electron Transfer in Molecular Electrocatalysis: Theoretical Methods and Design Principles. *Inorg. Chem.* **2014**, *53* (13), 6427–6443.
- (17) Klug, C. M.; Cardenas, A. J. P.; Bullock, R. M.; O'Hagan, M.; Wiedner, E. S. Reversing the Tradeoff between Rate and Over-

- 956 potential in Molecular Electrocatalysts for H₂ Production. *ACS Catal.*
957 **2018**, *8* (4), 3286–3296.
- 958 (18) Costentin, C.; Savéant, J.-M. Towards an Intelligent Design of
959 Molecular Electrocatalysts. *Nat. Rev. Chem.* **2017**, *1* (11), 0087.
- 960 (19) Mathew, S.; Yella, A.; Gao, P.; Humphry-Baker, R.; Curchod, B.
961 F. E.; Ashari-Astani, N.; Tavernelli, I.; Rothlisberger, U.; Nazeruddin,
962 M. K.; Grätzel, M. Dye-Sensitized Solar Cells with 13% Efficiency
963 Achieved through the Molecular Engineering of Porphyrin Sensitizers.
964 *Nat. Chem.* **2014**, *6* (3), 242.
- 965 (20) Ding, Y.; Zhang, C.; Zhang, L.; Zhou, Y.; Yu, G. Molecular
966 Engineering of Organic Electroactive Materials for Redox Flow
967 Batteries. *Chem. Soc. Rev.* **2018**, *47* (1), 69–103.
- 968 (21) Yang, C.; Ma, B. C.; Zhang, L.; Lin, S.; Ghasimi, S.; Landfester,
969 K.; Zhang, K. A. I.; Wang, X. Molecular Engineering of Conjugated
970 Polybenzothiadiazoles for Enhanced Hydrogen Production by
971 Photosynthesis. *Angew. Chem., Int. Ed.* **2016**, *55* (32), 9202–9206.
- 972 (22) Sieh, D.; Lacy, D. C.; Peters, J. C.; Kubik, C. P. Reduction of
973 CO₂ by Pyridine Monoimine Molybdenum Carbonyl Complexes:
974 Cooperative Metal-Ligand Binding of CO₂. *Chem. - Eur. J.* **2015**, *21*
975 (23), 8497–8503.
- 976 (23) Dey, S.; Mondal, B.; Chatterjee, S.; Rana, A.; Amanullah, S. K.;
977 Dey, A. Molecular Electrocatalysts for the Oxygen Reduction
978 Reaction. *Nat. Rev. Chem.* **2017**, *1* (12), 0098.
- 979 (24) Zhang, Z.; Yang, T.; Qin, P.; Dang, L. Nickel Bis (Dithiolene)
980 Complexes for Electrocatalytic Hydrogen Evolution: A Computa-
981 tional Study. *J. Organomet. Chem.* **2018**, *864*, 143–147.
- 982 (25) Koerstz, M.; Christensen, A. S.; Mikkelsen, K. V.; Nielsen, M.
983 B.; Jensen, J. H. High Throughput Virtual Screening of 230 Billion
984 Molecular Solar Heat Battery Candidates. *PeerJ. Phys. Chem.* **2021**, *3*,
985 No. e16.
- 986 (26) Sanchez-Lengeling, B.; Aspuru-Guzik, A. Inverse Molecular
987 Design Using Machine Learning: Generative Models for Matter
988 Engineering. *Science (Washington, DC, U. S.)* **2018**, *361* (6400), 360–
989 365.
- 990 (27) Schreier, M.; Luo, J.; Gao, P.; Moehl, T.; Mayer, M. T.; Grätzel,
991 M. Covalent Immobilization of a Molecular Catalyst on Cu₂O
992 Photocathodes for CO₂ Reduction. *J. Am. Chem. Soc.* **2016**, *138* (6),
993 1938–1946.
- 994 (28) Wang, J.; Gan, L.; Zhang, Q.; Reddu, V.; Peng, Y.; Liu, Z.; Xia,
995 X.; Wang, C.; Wang, X. A Water-Soluble Cu Complex as Molecular
996 Catalyst for Electrocatalytic CO₂ Reduction on Graphene-Based
997 Electrodes. *Adv. Energy Mater.* **2019**, *9* (3), 1803151.
- 998 (29) Li, X.; Liu, L.; Ren, X.; Gao, J.; Huang, Y.; Liu, B.
999 Microenvironment Modulation of Single-Atom Catalysts and Their
1000 Roles in Electrochemical Energy Conversion. *Sci. Adv.* **2020**, *6* (39),
1001 No. eabb6833.
- 1002 (30) Sun, L.; Reddu, V.; Fisher, A. C.; Wang, X. Electrocatalytic
1003 Reduction of Carbon Dioxide: Opportunities with Heterogeneous
1004 Molecular Catalysts. *Energy Environ. Sci.* **2020**, *13* (2), 374–403.
- 1005 (31) Zhang, X.; Wu, Z.; Zhang, X.; Li, L.; Li, Y.; Xu, H.; Li, X.; Yu,
1006 X.; Zhang, Z.; Liang, Y.; et al. Highly Selective and Active CO₂
1007 Reduction Electrocatalysts Based on Cobalt Phthalocyanine/Carbon
1008 Nanotube Hybrid Structures. *Nat. Commun.* **2017**, *8*, 14675.
- 1009 (32) Zhang, X.; Wang, Y.; Gu, M.; Wang, M.; Zhang, Z.; Pan, W.;
1010 Jiang, Z.; Zheng, H.; Lucero, M.; Wang, H. Molecular Engineering of
1011 Dispersed Electrocatalysts on Carbon Nanotubes for Selective CO₂
1012 Reduction. *Nat. Energy* **2020**, *5*, 684.
- 1013 (33) Liu, S.; Yang, H. B.; Hung, S.; Ding, J.; Cai, W.; Liu, L.; Gao, J.;
1014 Li, X.; Ren, X.; Kuang, Z.; et al. Elucidating the Electrocatalytic CO₂
1015 Reduction Reaction over a Model Single-Atom Nickel Catalyst.
1016 *Angew. Chem., Int. Ed.* **2020**, *59* (2), 798–803.
- 1017 (34) Wu, Y.; Jiang, Z.; Lu, X.; Liang, Y.; Wang, H. Domino
1018 Electrocatalysis of CO₂ to Methanol on a Molecular Catalyst.
1019 *Nature* **2019**, *575* (7784), 639–642.
- 1020 (35) Peterson, A. A.; Abild-Pedersen, F.; Studt, F.; Rossmeisl, J.;
1021 Nørskov, J. K. How Copper Catalyzes the Electrocatalysis of Carbon
1022 Dioxide into Hydrocarbon Fuels. *Energy Environ. Sci.* **2010**, *3* (9),
1023 1311–1315.
- (36) Frisch, M. J.; Trucks, G. W.; Schlegel, H. B.; Scuseria, G. E.; 1024
Robb, M. A.; Cheeseman, J. R.; Scalmani, G.; Barone, V.; Petersson, 1025
G. A.; Nakatsuji, H.; Li, X.; Caricato, M.; Marenich, A. V.; Bloino, J.; 1026
Janesko, B. G.; Gomperts, R.; Mennucci, B.; Hratchian, H. P.; Ortiz, J.; 1027
V.; Izmaylov, A. F.; Sonnenberg, J. L.; Williams-Young, D.; Ding, F.; 1028
Lipparini, F.; Egidi, F.; Goings, J.; Peng, B.; Petrone, A.; Henderson, 1029
T.; Ranasinghe, D.; Zakrzewski, V. G.; Gao, J.; Rega, N.; Zheng, G.; 1030
Liang, W.; Hada, M.; Ehara, M.; Toyota, K.; Fukuda, R.; Hasegawa, J.; 1031
Ishida, M.; Nakajima, T.; Honda, Y.; Kitao, O.; Nakai, H.; Vreven, T.; 1032
Throssell, K.; Montgomery, J. A., Jr.; Peralta, J. E.; Ogliaro, F.; 1033
Bearpark, M.; Heyd, J. J.; Brothers, E. N.; Kudin, K. N.; Staroverov, V.; 1034
N.; Kobayashi, R.; Normand, J.; Raghavachari, K.; Rendell, A.; Burant, 1035
J. C.; Iyengar, S. S.; Tomasi, J.; Cossi, M.; Millam, J. M.; Klene, M.; 1036
Adamo, C.; Cammi, R.; Ochterski, J. W.; Martin, R. L.; Morokuma, 1037
K.; Farkas, O.; Foresman, J. B.; Fox, D. J. *Gaussian 16*, revision A.03; 1038
Gaussian, Inc.: Wallingford CT, 2016. 1039
- (37) Adamo, C.; Barone, V. Toward Reliable Density Functional 1040
Methods without Adjustable Parameters: The PBE0Model. *J. Chem. 1041
Phys.* **1999**, *110* (13), 6158–6170. 1042
- (38) Grimme, S.; Ehrlich, S.; Goerigk, L. Effect of the Damping 1043
Function in Dispersion Corrected Density Functional Theory. *J. 1044
Comput. Chem.* **2011**, *32* (7), 1456–1465. 1045
- (39) Andrae, D.; Häußermann, U.; Dolg, M.; Stoll, H.; Preuß, H. 1046
Energy-Adjustedab Initio Pseudopotentials for the Second and Third 1047
Row Transition Elements. *Theor. Chim. Acta* **1990**, *77* (2), 123–141. 1048
- (40) Hariharan, P. C.; Pople, J. A. The Influence of Polarization 1049
Functions on Molecular Orbital Hydrogenation Energies. *Theor. 1050
Chim. Acta* **1973**, *28* (3), 213–222. 1051
- (41) Gordon, M. S. The Isomers of Silacyclopropane. *Chem. Phys. 1052
Lett.* **1980**, *76* (1), 163–168. 1053
- (42) Binning, R. C.; Curtiss, L. A. Compact Contracted Basis Sets 1054
for Third-row Atoms: Ga-Kr. *J. Comput. Chem.* **1990**, *11* (10), 1206– 1055
1216. 1056
- (43) Marenich, A. V.; Cramer, C. J.; Truhlar, D. G. Universal 1057
Solvation Model Based on Solute Electron Density and on a 1058
Continuum Model of the Solvent Defined by the Bulk Dielectric 1059
Constant and Atomic Surface Tensions. *J. Phys. Chem. B* **2009**, *113* 1060
(18), 6378–6396. 1061
- (44) Zhao, Y.; Schultz, N. E.; Truhlar, D. G. Design of Density 1062
Functionals by Combining the Method of Constraint Satisfaction with 1063
Parametrization for Thermochemistry, Thermochemical Kinetics, and 1064
Noncovalent Interactions. *J. Chem. Theory Comput.* **2006**, *2* (2), 364– 1065
382. 1066
- (45) Ho, J.; Klamt, A.; Coote, M. L. Comment on the Correct Use 1067
of Continuum Solvent Models. *J. Phys. Chem. A* **2010**, *114* (51), 1068
13442–13444. 1069
- (46) Lu, T.; Chen, F. Multiwfn: A Multifunctional Wavefunction 1070
Analyzer. *J. Comput. Chem.* **2012**, *33* (5), 580–592. 1071
- (47) Jeziorski, B.; Moszynski, R.; Szalewicz, K. Perturbation Theory 1072
Approach to Intermolecular Potential Energy Surfaces of van Der 1073
Waals Complexes. *Chem. Rev.* **1994**, *94* (7), 1887–1930. 1074
- (48) Turney, J. M.; Simonett, A. C.; Parrish, R. M.; Hohenstein, E. 1075
G.; Evangelista, F. A.; Fermann, J. T.; Mintz, B. J.; Burns, L. A.; Wilke, 1076
J. J.; Abrams, M. L.; Russ, N. J.; Leininger, M. L.; Janssen, C. L.; Seidl, 1077
E. T.; Allen, W. D.; Schaefer, H. F.; King, R. A.; Valeev, E. F.; Sherrill, 1078
C. D.; Crawford, T. D. Psi4: An Open-Source Ab Initio Electronic 1079
Structure Program. *Wiley Interdiscip. Rev. Comput. Mol. Sci.* **2012**, *2* 1080
(4), 556–565. 1081
- (49) Dunning, T. H., Jr Gaussian Basis Sets for Use in Correlated 1082
Molecular Calculations. I. The Atoms Boron through Neon and 1083
Hydrogen. *J. Chem. Phys.* **1989**, *90* (2), 1007–1023. 1084
- (50) VandeVondele, J.; Krack, M.; Mohamed, F.; Parrinello, M.; 1085
Chassaing, T.; Hutter, J. Quickstep: Fast and Accurate Density 1086
Functional Calculations Using a Mixed Gaussian and Plane Waves 1087
Approach. *Comput. Phys. Commun.* **2005**, *167* (2), 103–128. 1088
- (51) VandeVondele, J.; Hutter, J. Gaussian Basis Sets for Accurate 1089
Calculations on Molecular Systems in Gas and Condensed Phases. *J. 1090
Chem. Phys.* **2007**, *127* (11), 114105. 1091

- 1092 (52) Lippert, B. G.; Hutter, J.; Parrinello, M. A Hybrid Gaussian and
1093 Plane Wave Density Functional Scheme. *Mol. Phys.* **1997**, *92* (3),
1094 477–488.
1095 (53) Ishii, A.; Yamamoto, M.; Asano, H.; Fujiwara, K. DFT
1096 Calculation for Adatom Adsorption on Graphene Sheet as a
1097 Prototype of Carbon Nanotube Functionalization. *J. Phys. Conf. Ser.*
1098 **2008**, *100* (5), 052087.
1099 (54) Umadevi, D.; Sastry, G. N. Quantum Mechanical Study of
1100 Physisorption of Nucleobases on Carbon Materials: Graphene versus
1101 Carbon Nanotubes. *J. Phys. Chem. Lett.* **2011**, *2* (13), 1572–1576.
1102 (55) Grimme, S. Density Functional Theory with London
1103 Dispersion Corrections. *Wiley Interdiscip. Rev.: Comput. Mol. Sci.*
1104 **2011**, *1* (2), 211–228.
1105 (56) Grimme, S. XTB, a Tight-Binding Quantum Chemistry Code for
1106 Large Molecules; Universität Bonn, 2019.
1107 (57) Bannwarth, C.; Ehlert, S.; Grimme, S. GFN2-XTB An Accurate
1108 and Broadly Parametrized Self-Consistent Tight-Binding Quantum
1109 Chemical Method with Multipole Electrostatics and Density-Depend-
1110 ent Dispersion Contributions. *J. Chem. Theory Comput.* **2019**, *15* (3),
1111 1652–1671.
1112 (58) Weininger, D. SMILES, a Chemical Language and Information
1113 System. I. Introduction to Methodology and Encoding Rules. *J. Chem.*
1114 *Inf. Model.* **1988**, *28* (1), 31–36.
1115 (59) O'Boyle, N. M.; Banck, M.; James, C. A.; Morley, C.;
1116 Vandermeersch, T.; Hutchison, G. R. Open Babel: An Open
1117 Chemical Toolbox. *J. Cheminf.* **2011**, *3* (1), 33.
1118 (60) Yoshikawa, N.; Hutchison, G. R. Fast, Efficient Fragment-Based
1119 Coordinate Generation for Open Babel. *J. Cheminf.* **2019**, *11* (1), 49.
1120 (61) Kapusta, S.; Hackerman, N. Carbon Dioxide Reduction at a
1121 Metal Phthalocyanine Catalyzed Carbon Electrode. *J. Electrochem. Soc.*
1122 **1984**, *131* (7), 1511.
1123 (62) Dong, Q.; Zhang, X.; He, D.; Lang, C.; Wang, D. Role of H₂O
1124 in CO₂ Electrochemical Reduction As Studied in a Water-in-Salt
1125 System. *ACS Cent. Sci.* **2019**, *5* (8), 1461–1467.
1126 (63) Zagal, J. H.; Gulppi, M. A.; Cárdenas-Jirón, G. Metal-Centered
1127 Redox Chemistry of Substituted Cobalt Phthalocyanines Adsorbed on
1128 Graphite and Correlations with MO Calculations and Hammett
1129 Parameters. Electrocatalytic Reduction of a Disulfide. *Polyhedron*
1130 **2000**, *19* (22), 2255–2260.
1131 (64) Zagal, J. H.; Cárdenas-Jirón, G. I. Reactivity of Immobilized
1132 Cobalt Phthalocyanines for the Electroreduction of Molecular Oxygen
1133 in Terms of Molecular Hardness. *J. Electroanal. Chem.* **2000**, *489* (1),
1134 96–100.
1135 (65) Méndez-Hernández, D. D.; Tarakeshwar, P.; Gust, D.; Moore,
1136 T. A.; Moore, A. L.; Mujica, V. Simple and Accurate Correlation of
1137 Experimental Redox Potentials and DFT-Calculated HOMO/LUMO
1138 Energies of Polycyclic Aromatic Hydrocarbons. *J. Mol. Model.* **2013**,
1139 *19* (7), 2845–2848.
1140 (66) Sinnokrot, M. O.; Sherrill, C. D. Substituent Effects in $\Pi\text{-}\pi$
1141 Interactions: Sandwich and T-Shaped Configurations. *J. Am. Chem.*
1142 *Soc.* **2004**, *126* (24), 7690–7697.
1143 (67) Steinmann, S. N.; Sautet, P. Assessing a First-Principles Model
1144 of an Electrochemical Interface by Comparison with Experiment. *J.*
1145 *Phys. Chem. C* **2016**, *120* (10), 5619–5623.
1146 (68) Cao, H.; Xia, G.-J.; Chen, J.-W.; Yan, H.-M.; Huang, Z.; Wang,
1147 Y.-G. Mechanistic Insight into the Oxygen Reduction Reaction on the
1148 Mn-N₄/C Single-Atom Catalyst: The Role of the Solvent Environ-
1149 ment. *J. Phys. Chem. C* **2020**, *124* (13), 7287–7294.
1150 (69) Dance, I. The Correlation of Redox Potential, HOMO Energy,
1151 and Oxidation State in Metal Sulfide Clusters and Its Application to
1152 Determine the Redox Level of the FeMo-Co Active-Site Cluster of
1153 Nitrogenase. *Inorg. Chem.* **2006**, *45* (13), 5084–5091.